Research Square

Preprints are preliminary reports that have not undergone peer review.
They should not be considered conclusive, used to inform clinical practice,
or referenced by the media as validated information.

Investigation on laser-assisted ultra-precision cutting process technology for SiCp/Al composites

Peng Gu

gupeng@dhu.edu.cn

Donghua University

Zhongjin Luo
Daojie Hu
Andrea Mura
Chuanmin Zhu
Chengcheng Sun
Xiangjun Liu

Research Article

Keywords: SiCp/Al composites, laser-assisted machining, cutting mechanism, surface evaluation

Posted Date: July 2nd, 2026

DOI: https://doi.org/10.21203/rs.3.rs-9438065/v1

License: This work is licensed under a Creative Commons Attribution 4.0 International License.
Read Full License

Investigation on laser-assisted ultra-precision cutting process technology for SiCp/Al composites

Peng Gu[a] Zhongjin Luo[a] Daojie Hu[a] Andrea Mura[b] Chuanmin Zhu[c]
Chengcheng Sun[a] Xiangjun Liu [a*]
[a] College of Mechanical Engineering, Donghua University, Shanghai 201620, China
[b] Department of Mechanical and Aerospace Engineering, Politecnico di Torino, Torino 10129, Italy
[c] School of Mechanical Engineering, Tongji University, Shanghai 201804, China
✉Xiangjun Liu xjliu@dhu.edu.cn

Abstract: Medium-volume-fraction SiCp/Al composites are premier candidates for optical components, yet their application is constrained by severe surface defects like particle pull-out and interfacial debonding. To address these challenges, an optimized laser-assisted machining (LAM) strategy is employed. Distinct from purely mechanical assistants that primarily focus on force reduction, LAM leverages selective thermal softening to create a compliant buffer within the aluminum matrix, thereby reducing the surface roughness *Sa* to 0.023 μm. Utilizing constitutive models calibrated via quasi-static and high-temperature dynamic tests, finite element analysis reveals that LAM-induced thermal softening of the matrix reduces interfacial stress concentration and suppresses SiCp/Al interfacial debonding, minimizing particle pull-out and subsequent secondary plowing effects. Furthermore, a novel surface quality evaluation scheme utilizing reconstructed three-dimensional point clouds is developed to quantify cavity defects, effectively addressing the limitations of conventional roughness metrics.

Keywords: SiCp/Al composites; laser-assisted machining; cutting mechanism; surface evaluation

0 Introduction

Medium-volume-fraction SiCp/Al composites exhibit low density and high hardness, rendering them an ideal substrate material for applications such as space mirrors. As the application of medium-volume-fraction SiCp/Al composites in the optical field expands, increasingly stringent requirements are imposed on their surface quality. Precision fabrication regarding SiCp/Al composites possessing a medium volume fraction predominantly relies on grinding processes, which frequently introduce cavity defects on the surface, directly compromising optical performance. Consequently, a laser-assisted ultra-precision cutting process for SiCp/Al composite optical surfaces is proposed to mitigate cavity defects, thereby enhancing the surface quality of optical components.

Current processing techniques for SiCp/Al composites include milling, drilling, and grinding, with research focusing on machining characteristics, tool wear, deformation mechanisms, and surface quality. Huang S et al. [1-2] employed polycrystalline diamond tools to mill SiCp/Al composites, demonstrating that elevated speeds suppress built-up edges and burrs, though higher speeds increase compression on SiC reinforcements from the tool. Zhang K et al.[3] recently investigated the surface defects of SiCp/Al composites during the grinding process, confirming that particle pull-out and the resulting cavity defects inherently limit the ultimate surface quality achievable by conventional grinding. Gu P et al. [4] investigated the grinding features of 65vol.% SiCp/Al composites via diamond grit scratching experiments, constructing a forecasting framework for grinding resistance and thermal distribution with

under 10% deviation. Wang Y et al. [5] explored the fine-scale turning of 30 vol.% SiCp/Al composites, determining that tool contact with the top or center of particles causes stress-induced cracking, while underside engagement causes particle detachment, degrading surface quality. Xiang J et al. [6] performed drilling trials on 65 vol.% SiCp/Al composites, revealing that drilling depth dominates cutting force, which is strongly associated with edge defects. Cui Y et al. [7] simulated the milling of medium-volume-fraction SiCp/Al composites, assessing how tool geometry and cutting parameters influence cutting loads, thermal distribution, and chip generation. Chen S et al. [8] examined surface roughness fluctuations during machining, finding a 14.3%–30.7% finish improvement at cutting speeds of 100–400 mm/s due to modified particle removal and intensified plastic deformation. Lu S et al. [9] analyzed SiC particle arrangement during diamond turning, showing its critical influence on microscopic deformation and surface integrity. Overall, current studies have mainly concentrated on the conventional machining of SiCp/Al composites, while with the application of SiCp/Al composites in the ultra-precision field, research on ultra-precision machining remains relatively limited. In particular, the cutting-stress characteristics and their effects on particle deformation, fracture, and surface generation still require further systematic investigation.

Although optimizing tool geometry and cutting parameters mitigates some defects, these purely mechanical approaches have reached a bottleneck in suppressing brittle particle fracture. To overcome this, LAM strategy is adopted, which concentrates a laser beam ahead of the cutting tool to elevate local temperature, modifying mechanical properties for easier material removal[10-11]. Xu D et al. [12] focused on LAM for machining tungsten carbide, confirming its effectiveness in improving surface integrity and mitigating tool deterioration. Kim J et al. [13] applied LAM to cut high-hardness steel for microlens molds, showing reduced cutting loads and improved surface finish, though further modeling of parameter relationships is needed. Huang K et al. [14] explored LAM for ultra-precision cutting of mold steel, finding that LAM expanded the plastic cutting window, improved surface profile PV from 164 nm to 64 nm, and increased tool life by 29%. Liu Z et al. [15] applied LAM to single-point diamond nano-cutting targeting single-crystal silicon, demonstrating that the laser-assisted technique increased the ductile cutting depth threshold, reduced cutting forces, and mitigated wear on the cutter under suitable laser energy conditions. Zhang C et al. [16] explored laser-ultrasonic assisted turning (LUAT) of cemented carbide, analyzing cutting forces through modeling and experiments with a maximum prediction error of 18.6%. Taguchi optimization revealed amplitude as the most influential factor, with LUAT reducing cutting forces by 53.44%, 45.62%, and 21.64% compared to conventional, laser, and ultrasonic turning, respectively, while improving surface quality. Erdenechimeg K et al. [17] optimized LAM parameters for C/SiC composites using finite element analysis of cutting depth and Taguchi optimization targeting cutting loads and surface finish. Results indicated that cutting depth, preheating temperature, feed rate, and spindle speed significantly affected performance, with optimized parameters decreasing cutting resistance and enhancing surface integrity. You K et al. [18] compared conventional methods against the laser-assisted cutting strategy utilizing in-process heating (In-LAC) applied to binder-free tungsten carbide, employing both numerical and experimental approaches. In-LAC reduced cutting forces and subsurface damage, increasing the critical depth for crack-free surfaces from an initial 26.6 nm up to 106.3 nm. Optimal laser power (10-15 W) achieved a 4.66 nm roughness

value as well as extended tool longevity. Cui F et al. [19] showed that preheating in laser-assisted machining promotes thermal softening in SiCp/Al composites, enabling a transition from brittle fracture to ductile removal and thereby reducing subsurface damage. Lu X et al. [20] investigated the laser-assisted micro-milling of Inconel 718 through a fully thermo-mechanically coupled finite element model, demonstrating that appropriate laser pre-heating significantly reduces cutting forces and enhances the surface integrity of the superalloy. Overall, laser-assisted machining has shown significant potential for manufacturing process. It can effectively improve the surface quality. At present, there is limited research on laser-assisted ultra-precision processing of SiCp/Al composites, and further studies are urgently needed.

To address these gaps, a laser-assisted ultra-precision cutting strategy regarding optical-grade SiCp/Al composites is proposed in this study. The constitutive behavior of the composite material was experimentally determined using Split Hopkinson Pressure Bar tests, enabling accurate characterization under dynamic loading conditions. Based on the calibrated material model, a thermo-mechanically coupled three-dimensional finite element framework was established to investigate stress evolution, particle removal modes, and interfacial debonding behavior. Furthermore, three-dimensional topographic data of the machined optical surfaces were acquired and processed to reconstruct surface point clouds. A novel surface quality evaluation index specifically targeting cavity defects was proposed to quantitatively characterize defect size, density, and spatial distribution. Through the above research, the performance improvement effect of laser processing on SiCp/Al composites was revealed.

1 Experiment

1.1 Material properties

The workpiece employed is medium-volume-fraction SiCp/Al composites, produced via the powder metallurgical route. The matrix consists of the 6061 aluminum alloy. The silicon carbide reinforcements exhibit a mean size measuring 10 μm and a volumetric ratio of 45%. Subsequently, the preparation process and specimen shape pertaining to the SiCp/Al composite are illustrated in Fig. 1, including high-energy ball milling for uniform dispersion, cold pressing for compaction, and vacuum hot-press sintering for densification and bonding.

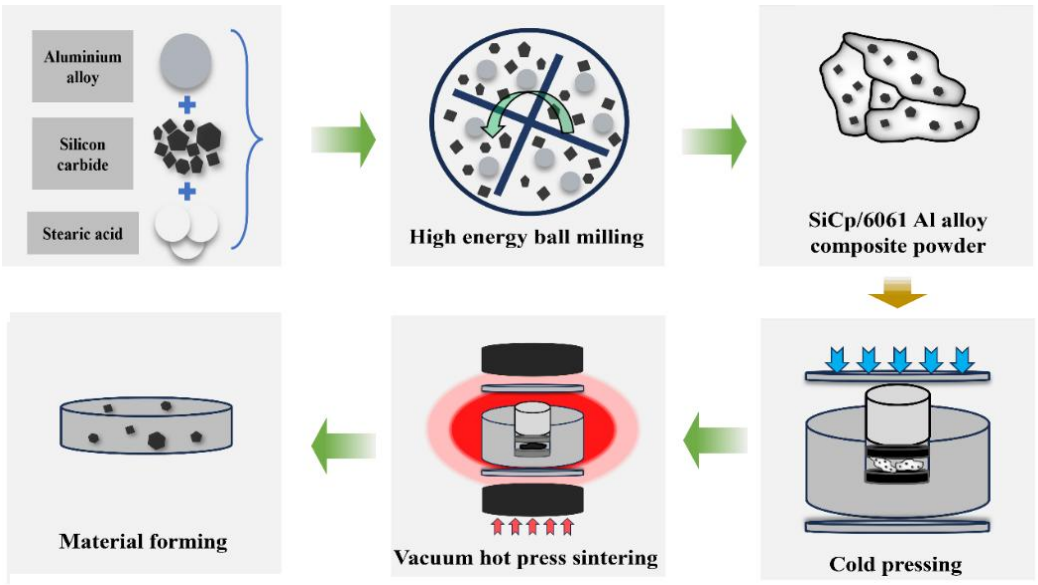


Fig. 1 Schematic diagram of the casting process for SiCp/Al composites

The elemental analytical findings are presented in Fig. 2 and Table 1. The fabricated SiCp/Al composite specimen mainly contains C, O, Al, and Si elements, supplemented by trace levels of Cu, Mg, and additional constituents. The primary material performance parameters of medium-volume-fraction SiCp/Al composites are presented in Table 1. The SiCp/Al composite exhibits hard and brittle behavior, attributed to its high elastic modulus and flexural strength. Nevertheless, its high thermal conductivity, low specific heat capacity, and enhanced thermal diffusivity facilitate efficient heat transfer during laser-assisted machining, thereby softening the material and optimizing cutting performance.

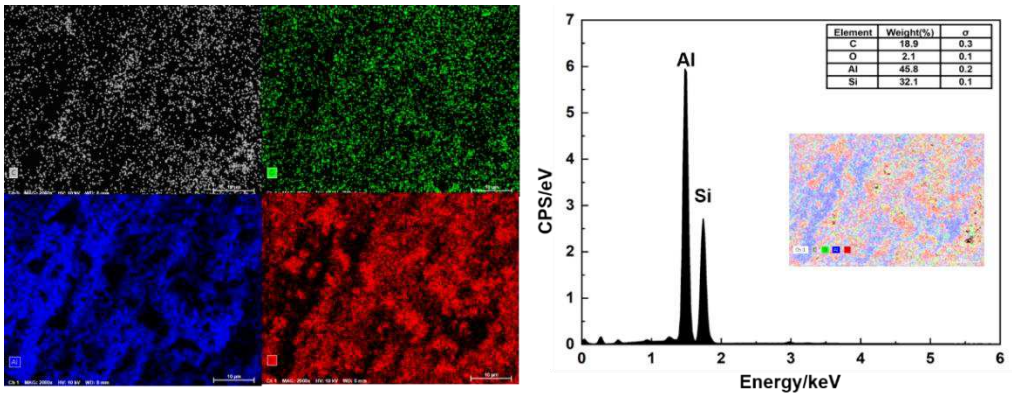


Fig. 2 Energy dispersive spectrum of SiCp/Al composites

Table 1 Mass fractions of chemical elements in 6061 aluminum alloy

Element	C	O	Si	Al	Others
Wt%	18.9	2.1	32.1	Balance	1.1

Table 2 Material performance parameters of SiCp/Al composites

Performance indicator	Elastic modulus (GPa)	Flexural strength (MPa)	Specific heat capacity (J/g·K)	Thermal conductivity (W/(m·K))	Density (g/cm^3)
Parameter	150	560	0.845	180	2.970

1.2 Experimental setup

The laser-assisted cutting experimental platform primarily comprises a laser heating assistance system and a single-point diamond-based turning device. A natural monocrystalline diamond (SCD) cutter was employed. The principal equipment is depicted in Fig. 1. The ultra-precision cutting machine employed is the Nanotech 250. A continuous-mode laser-assisted machining configuration was established, utilizing a laser integrated with a custom-designed collimator, which includes a protective lens, a focusing lens, and a collimator. The fiber laser model, YLR-300-MM-WC-Y11, operates in a constant-wave regime emitting at 1064 nm, featuring a spot radius measuring 0.014 mm, and uniform beam quality. The laser and tool tip are synergistically focused and aligned, enabling precise adjustments such as defocusing and tilt. The surface quality following ultra-precision cutting is evaluated using a white light interferometer. The mechanical sensor is fixed between the machine tool and the tool base to enable real-time acquisition of mechanical signals during cutting. When the laser is operational, the temperature during cutting is detected using an infrared pyrometer.

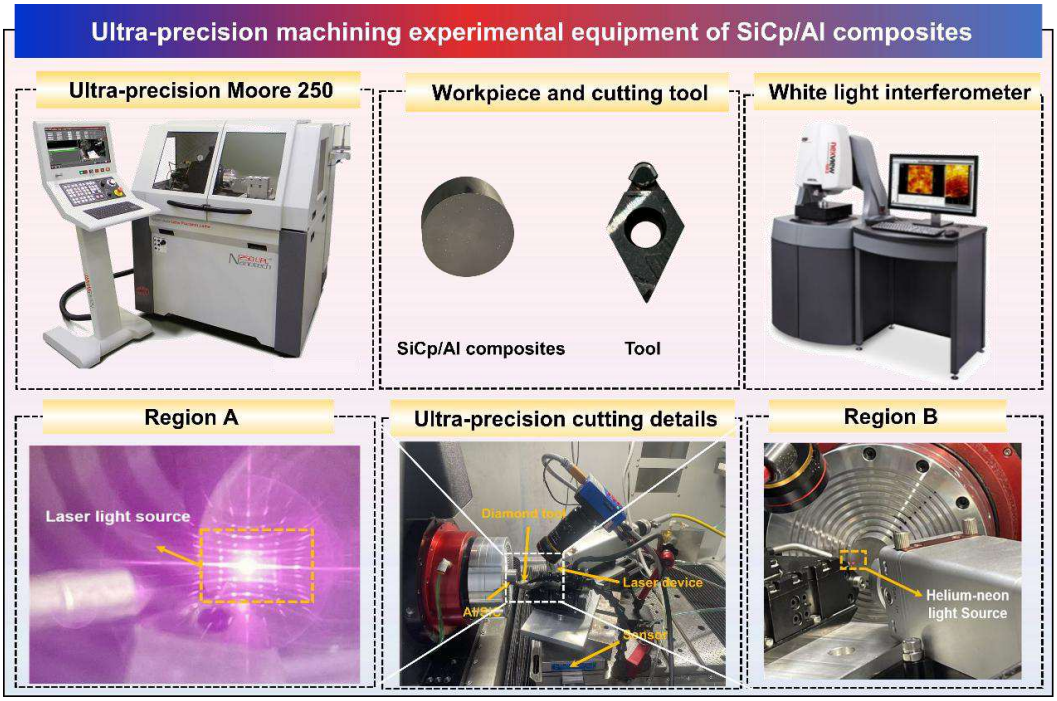


Fig. 3 Ultra-precision machining experimental equipment

1.3 Experimental process

The process parameters for continuous laser-assisted ultra-precision cutting of SiCp/Al composites primarily include spindle speed (n), feed rate (v_f), cutting depth (a_p), and laser power (P). Based on preliminary trials to determine suitable conditions, the spindle speed is set within 1000–2000 r/min, the feed rate within 1-3 mm/min, the cutting depth within 1-3 μm, and the laser power is kept constant at 50 W. Laser power selection must avoid extremes. Low power causes poor softening of the aluminum matrix, preventing effective reduction of cutting force and tool wear. Excessively high power, exceeding the melting temperature, leads to surface ablation, impairing quality.

The Box–Behnken Design (BBD) methodology is implemented with $k = 3$. This method efficiently covers the variable space using a three-level design, supports quadratic model fitting, and places experimental points at the midpoints of the edges of the variable space. Repeated center points enhance model reliability, making it suitable for this study. The experimental design is presented in Table 4, where experiments 1–12 are edge points, 13–16 are center points, and 17–18 are control groups without laser assistance.

Table 4 Box-Behnken Design (BBD) experimental table

Serial Number	n Coding	a_p Coding	v_f Coding	n(r/min)	a_p(μm)	v_f(mm/min)	P(w)
1	-1	-1	0	1000	1	2	50
2	+1	-1	0	2000	1	2	50
3	-1	+1	0	1000	3	2	50
4	+1	+1	0	2000	3	2	50
5	-1	0	-1	1000	2	1	50
6	+1	0	-1	2000	2	1	50

7	-1	0	+1	1000	2	3	50
8	+1	0	+1	2000	2	3	50
9	0	-1	-1	1500	1	1	50
10	0	+1	-1	1500	3	1	50
11	0	-1	+1	1500	1	3	50
12	0	+1	+1	1500	3	3	50
13	0	0	0	1500	2	2	50
14	0	0	0	1500	2	2	50
15	0	0	0	1500	2	2	50
16	0	0	0	1500	2	2	50
17	0	0	0	1500	2	2	0
18	0	0	0	1500	2	2	0

1.4 Experimental results

1.4.1 Surface topography

As shown in Fig. 4, a comparative analysis was conducted between conventional and laser-assisted ultra-precision cutting of SiCp/Al composites. Figs. 4(a) and (b) present the three-dimensional surface morphology obtained under conventional conditions, whereas Figs. 4(d) and (e) illustrate the surface characteristics under laser-assisted conditions. The surface machined without laser assistance exhibits evident cavities, irregular peaks, and discontinuities, while the laser-assisted surface appears significantly smoother with a reduced number and size of defects. Compared with the ordinary cutting surface, the surface after laser assisted processing shows obvious and regular parallel stripe-like textures. The *Sa* value of conventional cutting is 367.15 nm, while after adding laser, it drops to 23.56 nm. It can be seen that, while keeping other parameters consistent, introducing laser can significantly reduce the surface roughness, suggesting that laser exerts a consistent and evident influence on inhibiting surface peak and valley fluctuations and improving surface quality.

Under conventional cutting conditions, the material removal process is dominated by mechanical loading. Due to the elevated elastic modulus and brittle characteristics of the SiC particles, stress concentration readily develops within the particles when subjected to the compressive and shearing loads imposed by the diamond-based cutter. When the cutting force is at a moderate level, microcracks initiate and propagate inside the particles. The fragmented particles may remain partially embedded in the softened aluminum matrix, leaving behind residual cavities referred to as adherent pits. As the cutting force increases further, the interfacial adhesion stability between SiC particles and the aluminum matrix becomes insufficient to sustain the combined normal and shear stresses. Interfacial debonding then occurs, and these reinforcements undergo rotation, dislocate, and are eventually pulled out from the matrix, forming shedding pits and exposing the aluminum substrate on the machined surface.

Under laser-assisted conditions, localized preheating of the cutting zone significantly alters the thermo-mechanical response of the composite. The elevated temperature reduces the flow stress and yield strength of the aluminum matrix, thereby enhancing its plastic deformation capability and stress redistribution capacity. As a consequence, the overall cutting force is lowered and stress concentration at the particle-matrix interface is alleviated. The softened

matrix provides improved mechanical support to the embedded SiC particles, suppressing crack initiation and limiting crack propagation within the particles. Meanwhile, the reduction in interfacial stress decreases the likelihood of particle debonding and pull-out. This thermo-mechanical modification promotes a more stable and controlled material removal mode, leading to a significant decline in both adherent and shedding pits. The recorded enhancement of surface morphology therefore is attributed to the temperature-induced regulation of stress distribution and interfacial behavior, which will be further analyzed through coupled thermo-mechanical simulations in subsequent sections.

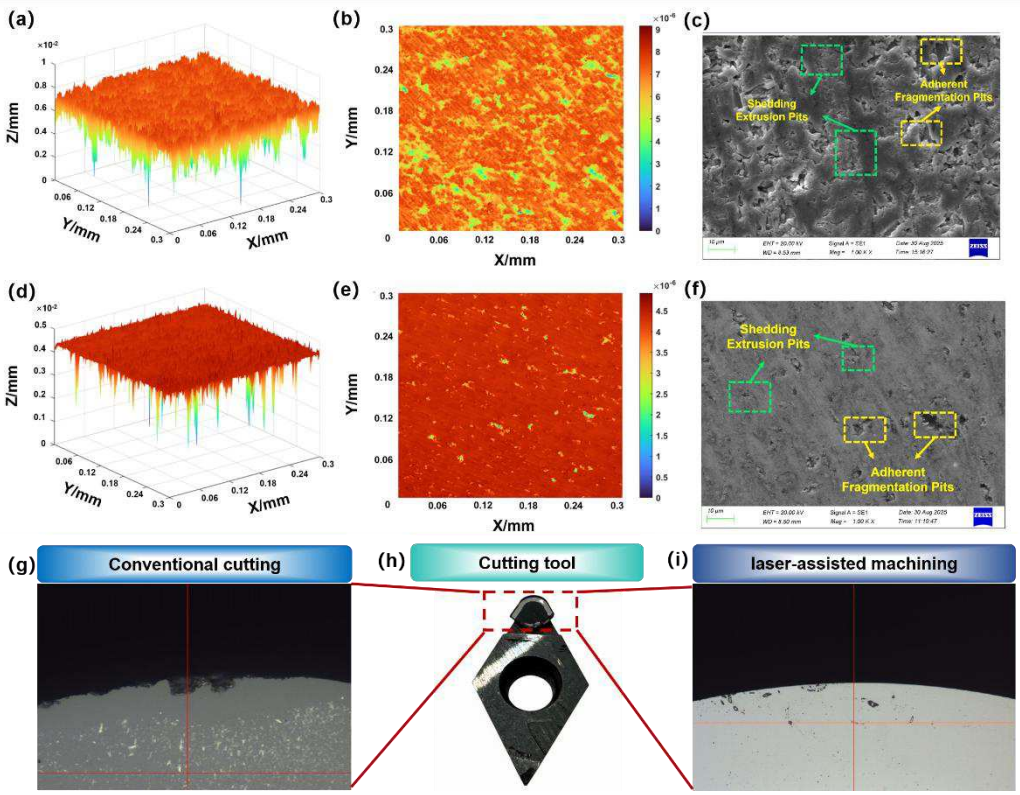


Fig. 4 Microstructures of conventional and laser-assisted machining surfaces ((a-c) conventional cutting (d-f) laser-assisted cutting (g-i) tool wear)

1.4.2 Wear of cutting tool

The wear characteristics of the diamond cutting tool under conventional and laser-assisted conditions are presented in Figs. 4(g) and 4(i), respectively. Under conventional cutting conditions, pronounced wear is observed at the tool tip arc region. The edge exhibits evident rounding and localized micro-chipping, indicating severe mechanical engagement between the cutter and the rigid SiC particles. Due to the high hardness and brittleness of SiCp/Al composites, large machining loads are induced across the tool–workpiece contact area during material removal. The repeated impact and abrasion caused by exposed SiC particles lead to accelerated tool wear, especially at the cutting edge where stress concentration is most significant.

In contrast, tool wear under laser-assisted cutting is noticeably reduced. The cutting edge retains a sharper geometry, and the extent of edge rounding and micro-fracture is significantly mitigated. The introduction of laser preheating modifies the cutting environment in two principal aspects. First, the heat-mediated softening of the aluminum substrate reduces its

plastic flow resistance, which lowers the overall cutting force and diminishes the mechanical burden sustained by the cutter. Second, the improved plasticity of the heated matrix enhances stress accommodation around SiC particles, reducing the severity of particle-tool impact and abrasive interaction.

It should be noted that laser parameters must be carefully controlled to ensure stable cutting performance. Excessive laser power may induce surface ablation or thermal damage, while insufficient power fails to provide adequate softening of the matrix. When optimized, laser-assisted cutting effectively reduces mechanical load and stabilizes the cutting process, thereby prolonging tool life. The reduction in tool wear not merely improves surface integrity consistency but furthermore contributes to enhanced processing productivity and reduced operational cost, highlighting the practical advantages of laser-assisted ultra-precision machining concerning SiCp/Al composites.

2 Laser-assisted ultra-precision cutting simulation

2.1 Establishment of laser-assisted ultra-cutting simulation model

In order to clarify the thermo-mechanical material removal kinetics in laser-assisted ultra-precision cutting of SiCp/Al composites, it is essential to formulate a precise constitutive framework capable of characterizing the material response under varying temperature and strain rate conditions. Since laser assistance introduces significant thermal effects and high strain rate deformation during cutting, the constitutive behavior of the aluminum matrix must account for work hardening, strain rate dependency, and thermal-induced softening. Therefore, a series of quasi-static tensile tests and high-temperature dynamic impact experiments were performed to derive the essential material constants for subsequent finite element simulations.

2.1.1 Material constitutive model of aluminum alloy

2.1.1.1 Static and quasi-static mechanical testing

The tensile test specimens were fabricated from aluminum alloy possessing a 2 mm thickness. The shape and measurements pertaining to the testing coupons are depicted in Fig. 5. Prior to the tension experiments, the exterior faces of the aluminum alloy samples were subjected to polishing with sandpaper to remove burrs and oxide layers from the surface and sides. Subsequently, a white base with black speckles was sprayed on the surface and sides. Finally, during the DIC test, the strain and displacement of the aluminum alloy matrix were determined based on the dynamic positions of the sprayed black speckles.

Fig. 6 illustrates the engineering stress-strain curves of the material under (a) static and (b) quasi-dynamic loading conditions. Both curves exhibit a distinct yield point, with variations in the strain rate during quasi-dynamic testing noticeably altering the yield strength. Furthermore, compared to the engineering stress-strain plots, the true stress-strain counterparts consistently display an upward trajectory. The distinct differences in true stress-strain behavior across varying strain rates during quasi-dynamic testing highlight a significant strain hardening effect within the aluminum alloy.

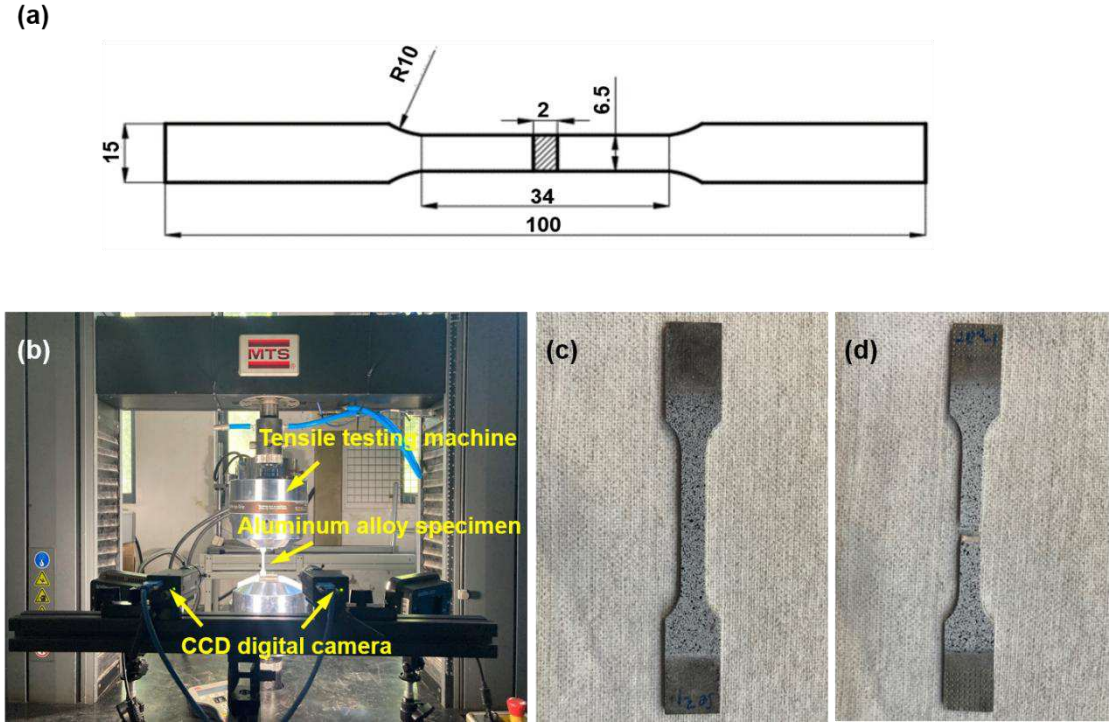


Fig. 5 Materials and setup ((a) Shape and dimensions of aluminum alloy specimens(b) DIC measurement system and CCD lens placement (c-d) aluminum alloy before and after testing)

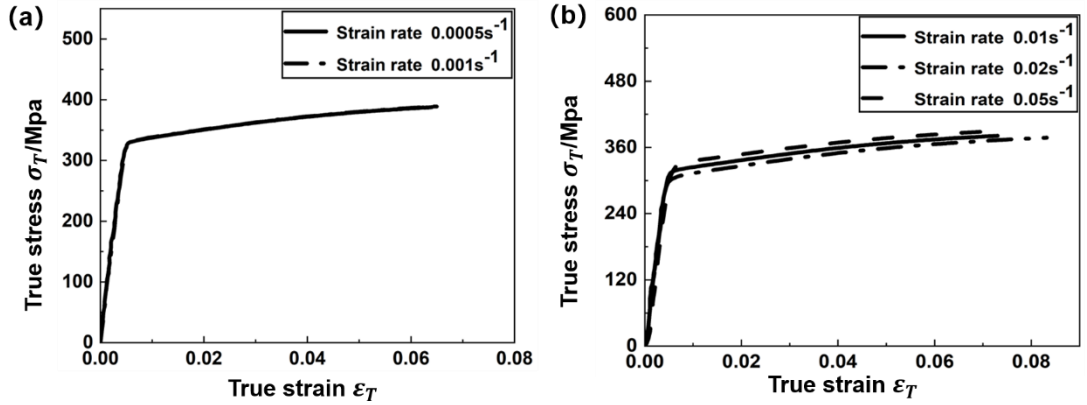


Fig. 6 Engineering and true stress-strain curves of aluminum alloy ((a) true stress-strain curve from static tensile testing (b) quasi-dynamic tensile testing)

2.1.1.2 Hopkinson bar dynamic testing and constitutive fitting

Fig. 7(a) is a schematic illustration of the Hopkinson bar experimental apparatus. The material shape for the Hopkinson dynamic tensile test is cylindrical, with specific dimensions shown in Fig. 7(b). The apparatus primarily is composed of an incident bar, a transmitter bar, a sleeve bullet, a signal acquisition system, and a buffer absorption device. By impacting the workpiece with the incident bar, the signal changes from strain gauges mounted on the incident as well as the transmission bars are obtained. Through a series of formula calculations, the true stress-strain profiles of the tensile workpiece at high strain rates can be derived. With an increase in strain rate, the intergranular slip fracture mechanism of the aluminum alloy becomes more pronounced, and the tensile fracture surface appears smoother.

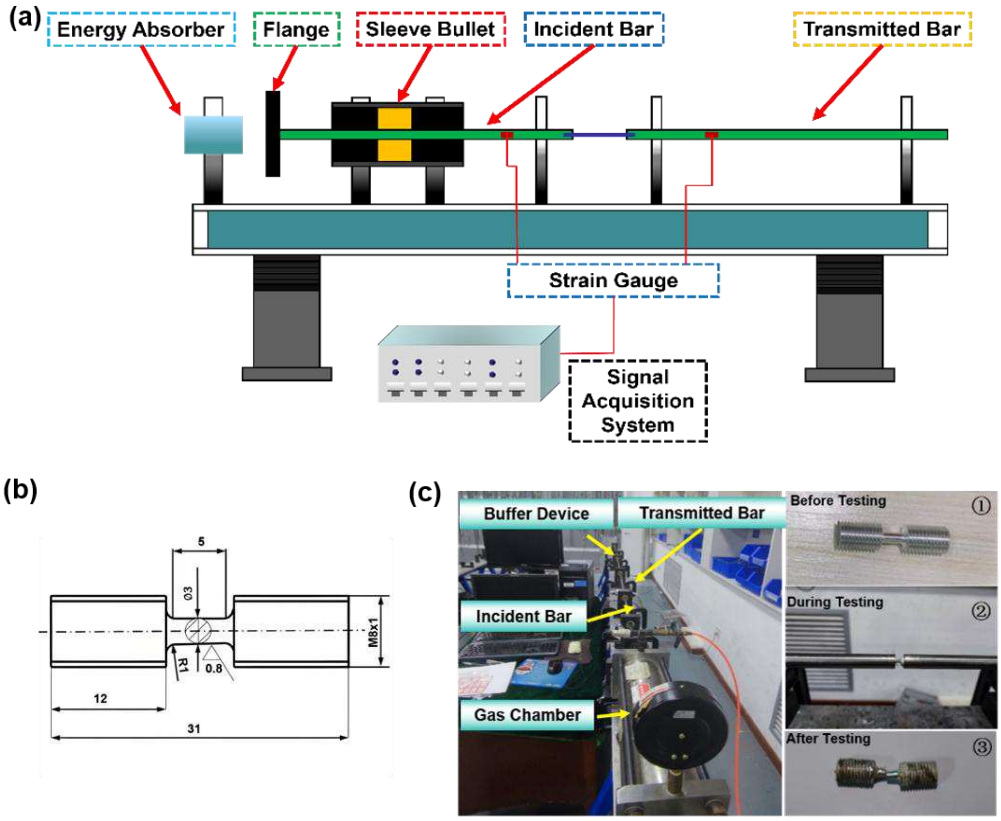


Fig. 7 Materials and setup ((a)(c) the hopkinson bar test apparatus (b) Dimensions of the specimen (d) Fracture morphologies of aluminum alloy under different strain rates)

Figs.8(a-d) present the true stress-strain curves at 25°C, 100°C, 200°C and 450°C, respectively, for strain rates of 750,1500, and 3000 s^{-1}. The results indicate that flow stress increases significantly with strain rate from 750 s^{-1} to 1500 s^{-1}, demonstrating pronounced strain rate hardening. As temperature rises from 25°C to 450°C, yield strength and flow stress decrease, while fracture elongation increases, reflecting enhanced ductility at higher temperatures. True stress-strain curves exhibit a steeper upward trend due to accounting for cross-sectional area reduction, indicating significant strain hardening.

During the high-speed tensile testing of aluminum alloy, compressed gas stored in the anterior chamber propels the sleeve bullet to impact the flange on the left side of the incident bar. Driven by the impact of the sleeve bullet, stress waves are induced in the incident bar, which propagate to the workpiece, inducing tensile loading. Strain gauges bonded to the incident and transmission bars record the waveforms of the incident, reflected, and transmitted waves. The true stress-strain relationships of the specimen are calculated based on the signals corresponding to the respective input, reflected, and output pulses.

Regarding the aluminum alloy matrix, the Johnson-Cook constitutive framework is widely applied to capture the mechanical response of metallic substances under large strain as well as elevated strain rate conditions, effectively characterizing the limiting strength and failure mechanisms of the aluminum matrix under extreme stress states. In the classical Johnson-Cook material mathematical equation, the flow stress is generally expressed as:

$$\sigma_{eq} = (A + B\varepsilon_{eq}^{\ n})(1 + C\ln\frac{\overset{g}{\varepsilon}}{\overset{g}{\varepsilon_0}})(1 - (\frac{T - T_{room}}{T_{melt} - T_{room}})^m) \quad (1)$$

where *A, B, C*, *n* and *m* are parameters of the Johnson-Cook material constitutive equation, σ_{eq} is the equivalent stress, ε_{eq} is the equivalent plastic strain, and $\dot{\varepsilon}$ is the reference strain rate. *T* is the reference temperature, and T_{melt} is the melting point of the material.

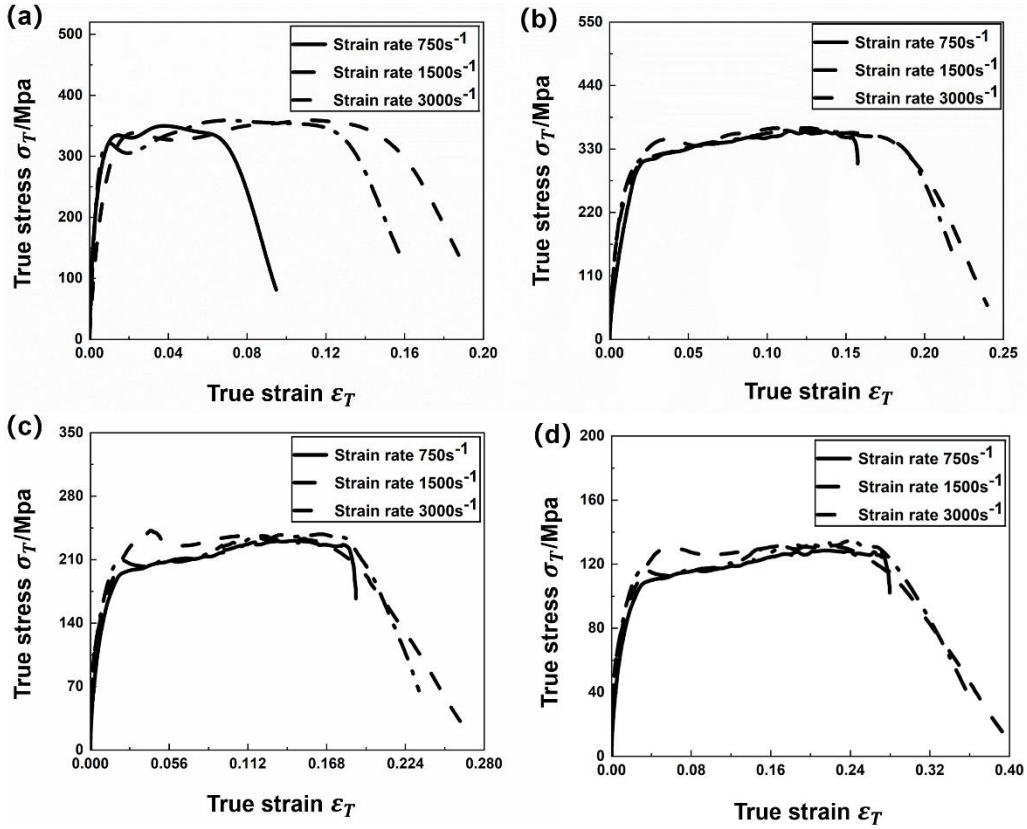


Fig. 8 Schematic of stress-strain curves and fracture morphologies at different temperatures ((a) 25℃ (b) 100℃ (c) 200℃ (d) 450℃)

Due to the obvious yield point in the true stress vs. strain curve pertaining to the aluminum alloy, the parameter *A* = 327.6 MPa can be obtained from the curve. By fitting the parameters *B* and *n* of the Johnson-Cook constitutive equation, the calibrated Johnson-Cook relation at static strain rate can be expressed as:

$$\ln(\sigma_{eq} - A) = n \ln \varepsilon_{eq} + \ln B \tag{2}$$

After a series of data fittings, the parameters *B* =891.36 and *n* =0.9401 in the Johnson-Cook material constitutive equation are obtained. At room temperature, the high-speed compression test using the Hopkinson pressure bar is very brief, and the Johnson-Cook material constitutive equation for aluminum alloy is transformed into:

$$\sigma_{eq} = (327.6 + 891.36\varepsilon_{eq}^{\ 0.9401})\left(1 + C \ln \frac{\dot{\varepsilon}}{\dot{\varepsilon}_0}\right)(1 - (\frac{T - T_{room}}{T_{melt} - T_{room}})^m) \tag{3}$$

By fitting the stress vs. strain profiles of the aluminum alloy across varying strain rates, the *C* values associated with distinct strain rates are derived, and subsequently their average value is taken to obtain the *C* value of 0.00678 in the Johnson-Cook constitutive formulation characterizing the aluminum matrix.

The Johnson-Cook material constitutive equation for aluminum alloy is transformed into:

$$\sigma_{eq} = (325.66 + 794.172\varepsilon_{eq}^{0.894})\left(1 + 0.00678\ln\frac{\dot{\varepsilon}}{\dot{\varepsilon}_0}\right)(1 - (\frac{T - T_{room}}{T_{melt} - T_{room}})^{m}) \quad (4)$$

Subsequently, the dynamic tensile experimental data obtained at elevated temperatures were incorporated into the constitutive model to determine the parameter *m* through a series of iterative fittings, ultimately yielding a value of *m*=0.8576.

Consequently, the determined Johnson-Cook constitutive relation describing the aluminum alloy is expressed as:

$$\sigma_{eq} = (325.66 + 794.172\varepsilon_{eq}^{0.894})\left(1 + 0.00678\ln\frac{\dot{\varepsilon}}{\dot{\varepsilon}_0}\right)(1 - (\frac{T - T_{room}}{T_{melt} - T_{room}})^{0.8576}) \quad (5)$$

The parameters d_1-d_5 represent the material failure model parameters, and the corresponding Johnson-Cook fracture criterion coefficients for the specific aluminum alloy matrix are listed in Table 5 [21].

Table 5 Johnson-cook fracture criterion parameters for aluminum matrix material

d_1	d_2	d_3	d_4	d_5
0.13	0.13	-1.5	0.011	0

2.1.2 Material constitutive model of silicon carbide

Silicon carbide particles are characterized as rigid and fragile substances, and the stress-strain relationship of such hard-brittle materials may be characterized via the Johnson-Holmquist (JH) constitutive relation. When the principal stress within silicon carbide exceeds the critical tensile limit, the SiC particles undergo fragmentation. The maximum normal stress criterion facilitates the determination of the onset and location of fracture [22], with the relevant equation presented as:

$$\max(\sigma_1, \sigma_2, \sigma_3) = \sigma_b \quad (6)$$

where $\sigma_1, \sigma_2, \sigma_3$ represent the principal stresses along the three directions, and σ_b denotes the tensile strength of silicon carbide. As the fracture process initiates in SiC particles, an energy-based criterion is utilized to regulate the progression of failure behavior, with the crack displacement u_{n0} expressed as:

$$u_{n0} = 2G_f^I / \sigma_m^I \quad (7)$$

where G_f^I represents the mode I fracture energy of silicon carbide particles, and σ_m^I denotes the failure stress associated with the formation of mode I cracks. The shear modulus of SiC particles during the failure evolution phase is designated as G_s, which is defined as:

$$G_s = \rho(\varepsilon_{nn}^{ck})G \quad (8)$$

$$\rho(\varepsilon_{nn}^{ck}) = (1 - \frac{\varepsilon_{nn}^{ck}}{\varepsilon_{\max}^{ck}})^{\rho} \quad (9)$$

where G represents the shear modulus of silicon carbide, $\rho(\varepsilon_{nn}^{ck})$ denotes the shear

retention coefficient, ε_{nn}^{ck} indicates the cracking strain, ρ and $\varepsilon_{\max}^{ck}$ are material property parameters of silicon carbide. The Johnson-Holmquist constitutive equation and fracture criterion parameters for silicon carbide particles are shown in Table 6[22].

Table 6 Johnson-holmquist fracture criterion parameters for silicon carbide particles

σ_b/MPa	G_f^I/(J/m^2)	ρ	$\varepsilon_{\max}^{ck}$
1500	30	1	0.001

2.1.3 Material constitutive model of interface

In the cutting simulation, the transmission of stress and strain at the interface, material properties, and damage forms are crucial. To reflect the bonding-sliding effect and interaction between the reinforcing silicon carbide particle reinforcement phase and the aluminum host matrix, a cohesive zone model is adopted to represent the interfacial region. The failure process of the interface phase primarily consists of two steps: under external stress, the displacement of separation expands alongside the rising stress localized at the interface, and damage initiates when the separation displacement attains the critical damage initiation limit δ_{init}. With the sustained growth of separation displacement, stress levels start to decline, marking the transition of the interface phase into the damage progression regime. When the separation displacement attains the critical failure limit δ_{max}, the stress magnitude diminishes to zero, resulting in total interfacial decohesion. The relationship curve of normal stress and separation displacement is shown in Fig. 9. The parameters of the mixed linear cohesive-sliding weak interface layer constitutive model between silicon carbide and aluminum alloy are shown in Table 7[23].

Table 7 Interface layer constitutive model parameters

K_{nn}	δ_n^{init}	$\delta_n^{\max}$
6.9e^{11}	0.001	0.006

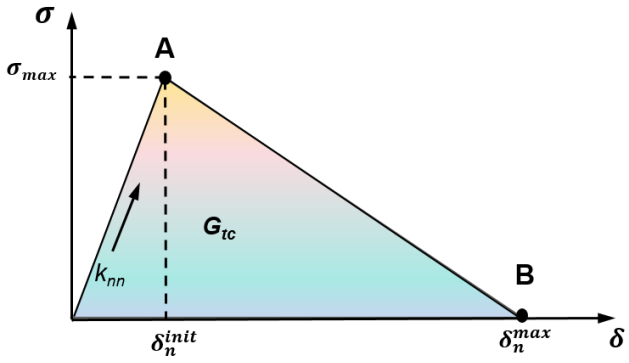


Fig. 9 Relationship curve of normal stress and separation displacement

2.2 Simulation process analysis of laser-assisted ultra-cutting process

2.2.1 Analysis of ultra-cutting simulation model

Within the SiCp/Al composite structure, silicon carbide particles appear irregularly and randomly scattered throughout the aluminum host. A Python script is used to set the volume fraction, particle area range, and external shape, establishing a finite element framework with stochastically dispersed polygonal particles in Abaqus. This model accounts for particle fracture, matrix deformation failure, and incorporates cohesive elements to simulate the bonding failure between the matrix and particles, more accurately reflecting particle failure during cutting. A

heat flux function defining non-uniform energy distribution, incorporating parameters such as position, time, power, and moving speed, was developed using Visual Studio and Fortran. By setting relevant parameters, a laser thermal source is capable of being incorporated during machining operations on SiCp/Al composites in order to simulate the operating conditions of laser-assisted cutting in actual machining, thereby the cutting model is established.

The conduction process associated with the laser thermal source across the specimen exterior is depicted in Fig. 10(a) and (b). As illustrated in Fig. 10(c), a finite element model for the SiCp/Al composites was established with randomly distributed silicon carbide particles. The workpiece dimensions are 0.25 mm in breadth and 0.1 mm in altitude. These SiC particles, possessing an average dimension of nearly 10 μm, are stochastically dispersed within the aluminum matrix. The model comprises a total of 18440 mesh elements. The diamond cutter features a 0° rake angle. In light of the vastly superior hardness of diamond relative to the SiCp/Al composites, structural distortion of the tool throughout the material removal phase is discounted, and the cutter is treated as a rigid body.

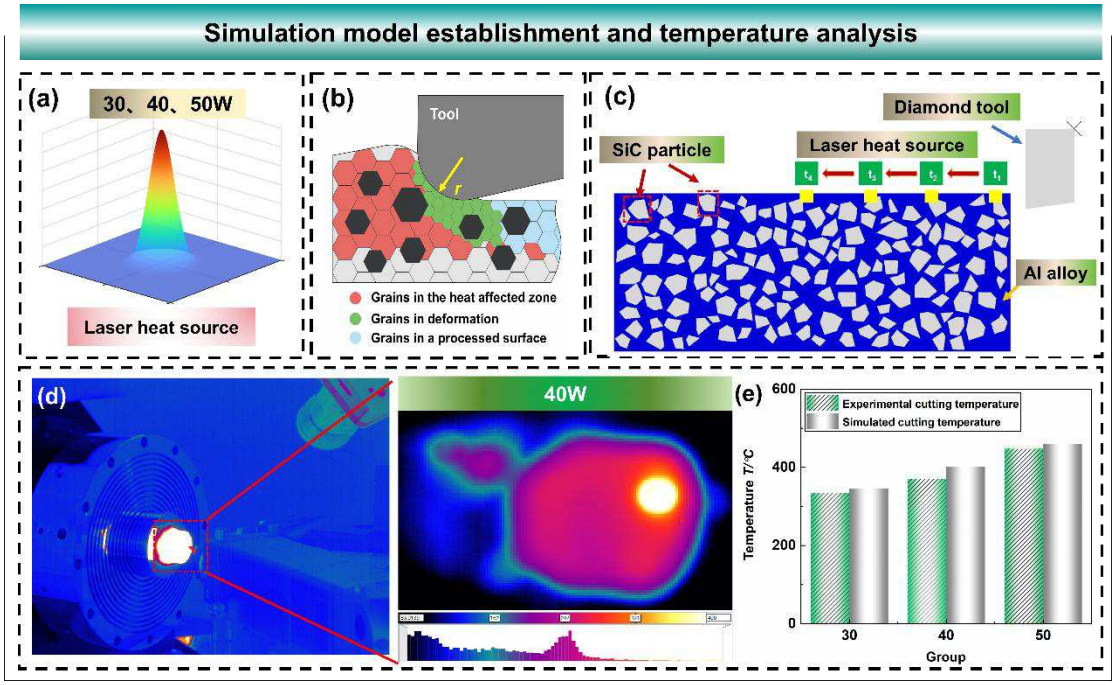


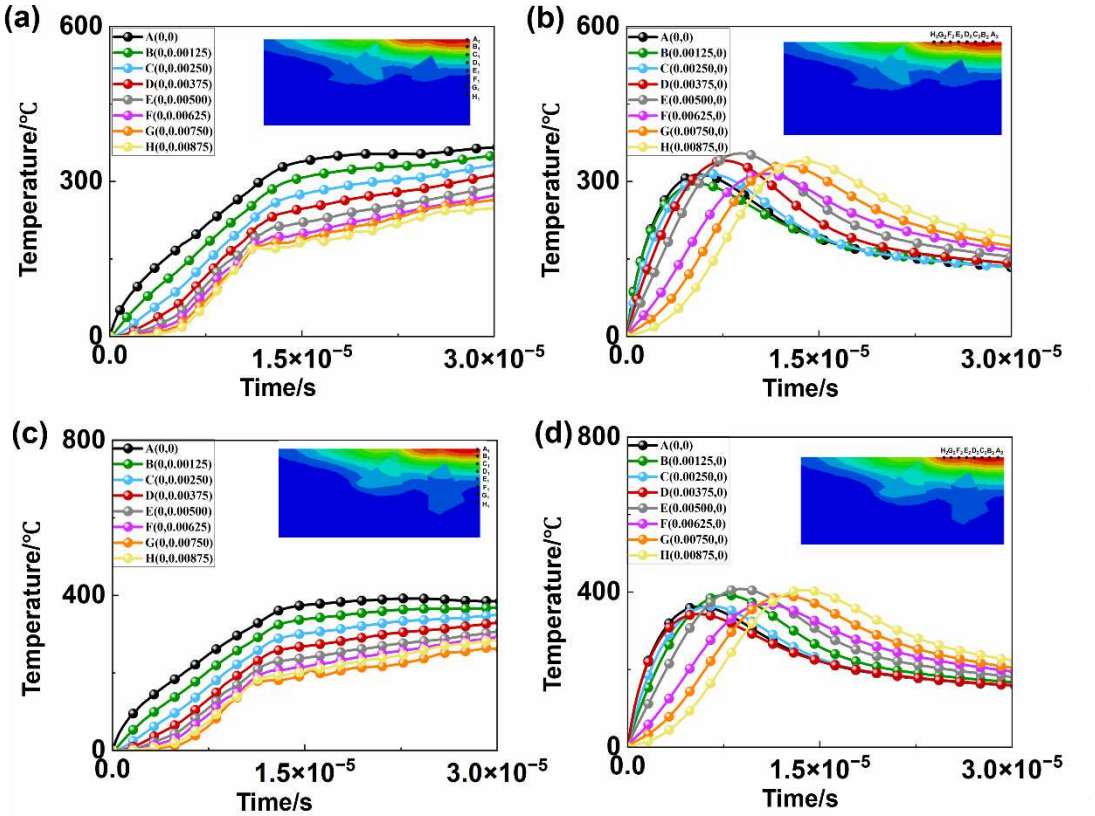
Fig. 10 Schematic of laser-assisted cutting simulation ((a) heat source (b)laser added on the surface (c) finite element model (d) the temperature field distribution (e) the experimental and simulated temperature under different laser powers)

2.2.2 Temperature analysis of ultra-cutting process

Throughout laser-aided ultra-precision machining, the interplay between the laser irradiation and the workpiece results in localized thermo-mechanical coupling. The absorbed laser energy is primarily converted into heat at the irradiated surface and subsequently transferred into the interior of the material. Due to the short interaction time and relatively high thermal conductivity of the aluminum matrix, heat conduction dominates the energy transfer process, while convective and radiative heat losses from the surface to the surrounding environment play secondary roles. The spatial distribution of the laser energy is modeled as a Gaussian heat source, generating a concentrated high-temperature zone at the irradiation center. As the laser beam scans across the workpiece surface, the heat source moves continuously,

leading to the formation of a transient and non-uniform temperature field. This dynamic thermal loading produces a significant temperature gradient along both the scanning direction and the depth direction. To validate the thermal simulation model, infrared thermography measurements were conducted using a Telops m400x infrared thermal imaging system. The thermal profiles across the surface during laser exposure were recorded at incident laser power levels of 30 W, 40 W, and 50 W. The experimentally measured temperature fields are presented in Fig. 10(d). The results indicate that the maximum surface temperature increases significantly with laser power in Fig. 10(e). At 30 W, the peak temperature reaches approximately 345 °C; at 40 W, it increases to around 383 °C; and at 50 W, it approaches 440 °C. The comparison between experimentally measured peak temperatures and numerically simulated values shows good agreement, with only minor deviations.

The corresponding temperature field distributions are presented in Fig. 11. Eight observation nodes were uniformly selected in both the vertical and horizontal directions within the heat-affected zone to monitor the temporal evolution of temperature during laser irradiation. The results demonstrate that the temperature distribution exhibits a stepped gradient pattern, with rapid attenuation away from the irradiation center. As laser power increases, both the peak temperature and the spatial extent of the heat-affected zone expand significantly. The elevated temperature promotes thermally-induced softening of the aluminum matrix, thereby reducing its flow stress and facilitating plastic deformation during cutting. However, excessive laser power may induce localized overheating or surface ablation, which can deteriorate surface integrity and dimensional accuracy. Therefore, optimization of laser parameters is essential to attain an equilibrium between heat-mediated softening and surface quality control in laser-assisted ultra-precision cutting.



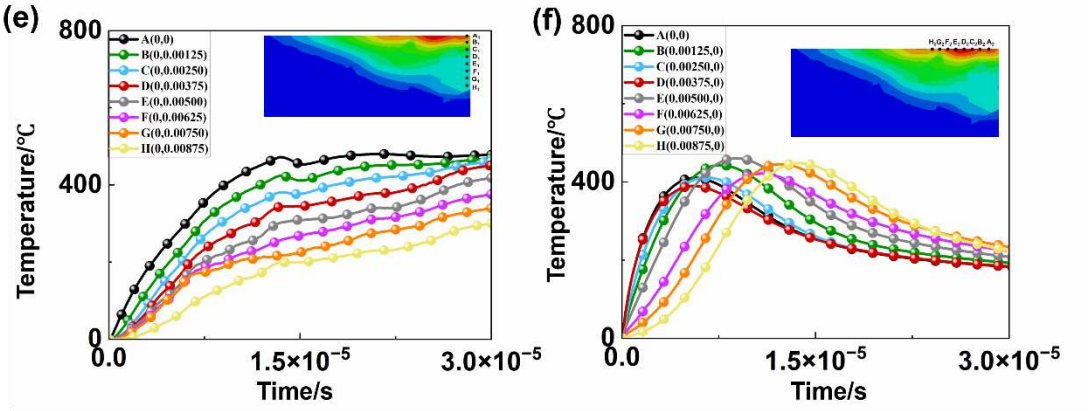


Fig. 11 Schematic of simulated temperature distribution ((a-b) 30W (c-d) 40W (e-f) 50W)

2.2.3 Material removal analysis of ultra-cutting process

During the cutting process, the interaction between the tool and the SiC reinforcements can be categorized into three scenarios based on the tool trajectory: engagement with the upper half, the lower half, or the center of the particle. Fig. 12(a) illustrates the interaction mechanics as the cutter engages the superior region of a SiC particle. Under conventional cutting, the tool trajectory induces significant torque, causing particle rotation and interfacial debonding. The uprooted particle is frequently trapped and dragged by the tool flank, pressing into the machined surface to create deep pits and exacerbate subsurface damage. Conversely, under laser-assisted machining, thermal softening of the aluminum matrix dampens vibration impacts and alleviates localized stress concentrations. As the tool traverses the upper portion, the segment above the path fractures and is removed with the chip, while the lower section remains securely anchored.

Fig. 12(b) illustrates the material removal mechanism when the tool trajectory aligns with the mid-height of the SiC particle. Under conventional cutting, intense compression and interfacial shear trigger premature debonding. Once interfacial integrity is compromised, the particle loses lateral constraint and is driven forward by the rake face as a hard third-body abrasive, causing secondary micro-ploughing and scratching. This migration intensifies localized material displacement and expands cavity defects. Under laser-assisted machining, thermal softening enhances plastic accommodation and homogenizes contact stress, effectively suppressing debonding. As the tool traverses the particle, the segment above the path fractures and is evacuated, while the lower segment remains anchored by the matrix support. This suppresses deleterious particle transport along the rake face, yielding a superior surface finish with fewer topographical defects.

Fig. 12(c) illustrates the engagement between the cutter and the inferior region of a SiC particle. Under conventional cutting, the combination of compressive stress and rigid matrix confinement leads to particle fracture and uprooting. The particle is forcibly pulled out and plows upward into the matrix, causing substantial plastic deformation and severe subsurface damage. Under laser-assisted machining, matrix softening reduces rigidity, facilitating a uniform stress distribution and mitigating localized concentrations. Thermal intervention alleviates stresses at the tool-SiC interface, reducing the likelihood of fragmentation and debonding. Furthermore, the laser-mediated rheological flow enables smoother material removal while maintaining interfacial stability.

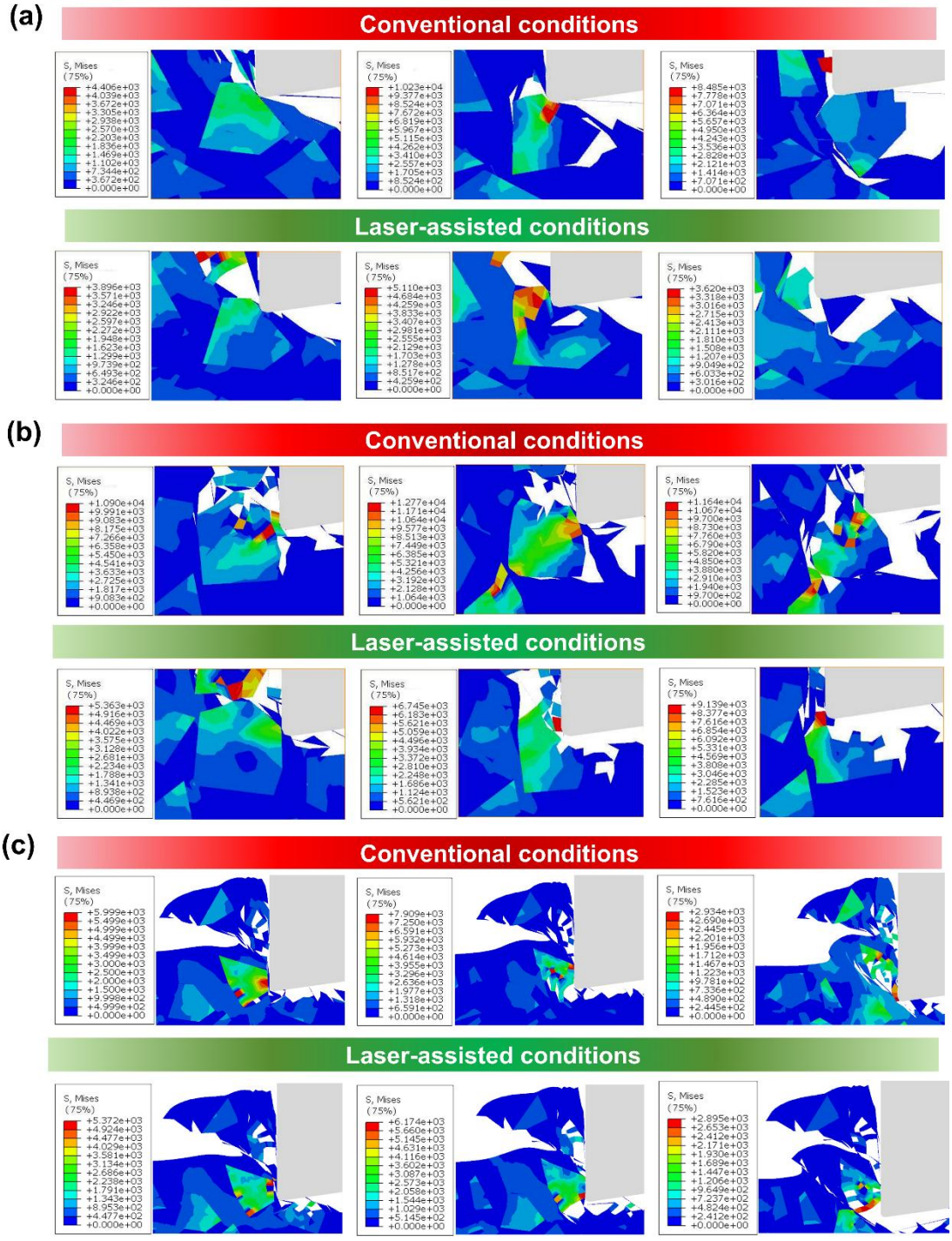


Fig. 12 Schematic of simulated cutting process ((a) upper cutting position (b) mid-range cutting position (c)lower cutting position)

2.2.4 Cutting stress analysis of ultra-cutting process

As illustrated in Fig. 13(a), the stress distribution in the aluminum matrix under conventional and laser-assisted cutting conditions is compared. Under conventional conditions, the stress in the aluminum matrix exhibits a radial distribution pattern, with the maximum stress at the tool–workpiece direct contact point reaching approximately 800 MPa, while stresses in other cutting regions range from 400 to 530 MPa. In contrast, under laser-assisted conditions, the central contact stress is significantly reduced to approximately 380 MPa, with stresses in

surrounding regions ranging from 170 to 300 MPa, indicating a marked improvement relative to conventional conditions. After the tool departs from the machined surface, residual stresses emerge in the aluminum matrix, averaging approximately 230 MPa under conventional conditions and approximately 110 MPa under laser-assisted conditions. The thermal softening induced by the laser mitigates residual stresses in the aluminum matrix, thereby preventing the propagation of pre-existing microcracks and further damage to the machined surface. Subsequent analysis focuses on the stress distribution at the tool–silicon carbide particle interface in Fig. 13(b).

Under conventional conditions, the extrusion effect of the rigid aluminum matrix generates a pre-stress of approximately 600 MPa on the particle before direct tool-particle contact. Upon tool engagement, the stress escalates rapidly; once the interfacial stress between the particle and the surrounding matrix reaches approximately 2000 MPa, interfacial failure occurs, leading to particle debonding. As the tool advances further, the debonded particle undergoes rotation driven by the tool tip and enters the flank contact zone, triggering severe subsurface damage. In contrast, under laser-assisted conditions, the thermally-induced softening of the matrix reduces the extrusion stress to approximately 400 MPa with suppressed fluctuations. The interfacial stress is significantly lowered to about 1000 MPa, which effectively maintains the integrity of the particle–matrix bond and inhibits premature debonding. As the tool continues to advance, the enhanced plastic flowability of the matrix facilitates a stable stress transition, allowing the SiC particles to be directly sheared by the cutting edge, thereby preventing subsequent subsurface damage typically induced by particle tumbling.

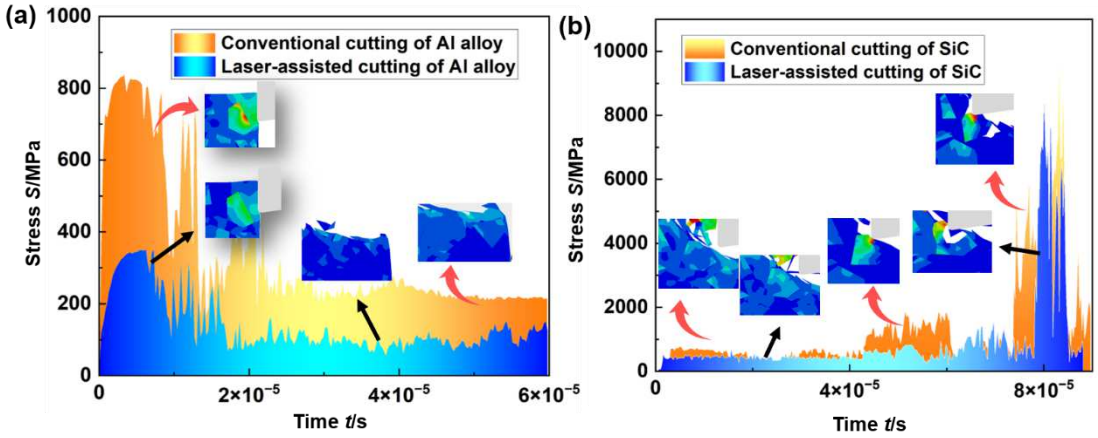


Fig. 13 Schematic of simulated cutting stress of SiCp/Al composites((a) matrix (b) particles)

2.2.5 Surface analysis of ultra-cutting process

After completion of the cutting simulations, the surface morphology was analyzed and compared under both conventional cutting and laser-assisted machining conditions in Fig. 14. Under conventional cutting conditions, the aluminum matrix undergoes severe plastic deformation due to high cutting forces and strong constraint imposed by embedded SiC particles. When the cutting tool encounters a hard SiC reinforcement, stress concentration develops at the particle-matrix interface. If the interfacial shear stress exceeds the bonding strength, partial debonding initiates and propagates along the interface. Subsequent tool advancement results in complete particle extraction, leaving a cavity that geometrically resembles the particle morphology. In addition, dislodged fragments may become entrapped between the tool and the machined surface, producing indentation-type defects. Matrix tearing

is primarily associated with the mismatch in mechanical properties between the ductile aluminum matrix and brittle SiC particles. The localized obstruction of plastic flow by rigid particles generates high tensile stress in the surrounding matrix, leading to tearing and surface discontinuities.

In contrast, under LAM conditions, laser-induced thermal softening reduces the flow stress of the aluminum matrix and enhances plastic compatibility across the tool–particle–matrix interaction zone. The reduced cutting force mitigates stress concentration and lowers peak interfacial shear stress. As a result, the probability of particle pull-out and large-scale interfacial debonding is significantly decreased. Moreover, improved plastic accommodation suppresses matrix tearing and limits subsurface crack propagation. Although localized particle crushing may still occur, the overall removal process becomes more controlled, leading to a smoother surface with fewer cavities and reduced subsurface damage. These results indicate that laser assistance modifies the stress distribution and interfacial failure mode during cutting, thereby improving surface integrity.

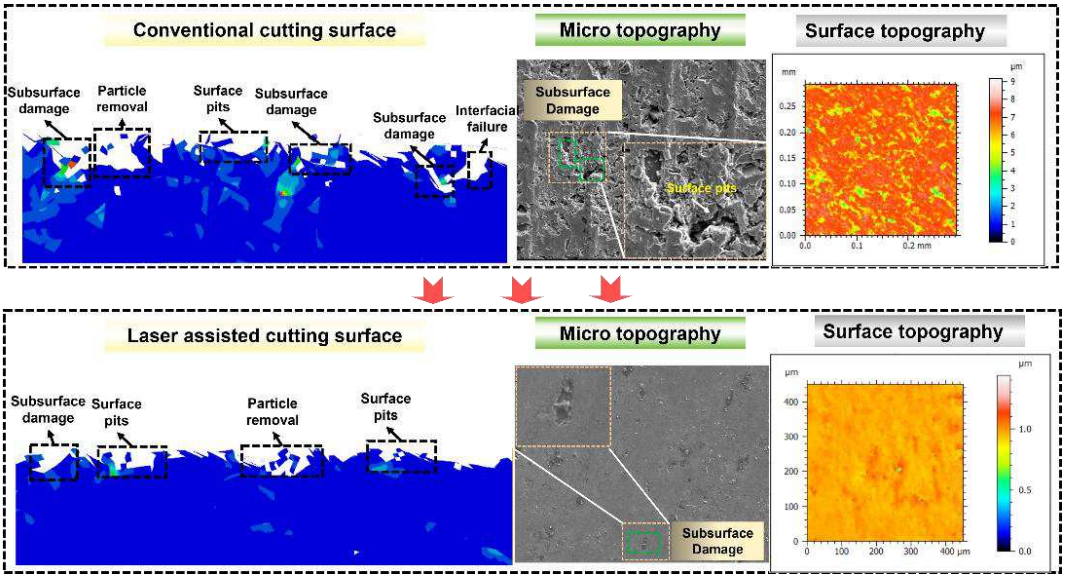


Fig. 14 Surface morphology after cutting((a) conventional cutting (b) laser assisted cutting)

3 Surface evaluation after laser-assisted ultra-precision cutting process

3.1 Surface evaluation process

To facilitate the optimization of processing parameters in laser-assisted machining, an effective surface assessment approach is required. As traditional roughness metrics may not fully capture localized defects in composites, a quality evaluation index based on 3D point cloud analysis is introduced to quantitatively characterize surface integrity.

3.1.1 Characterization method for cavity defects

Fig. 15(a) presents a schematic diagram illustrating a method for characterizing cavity defects. Here, P_B represents the lowest point of the three-dimensional contour, while P_T denotes the highest point. P_A corresponds to the height with the maximum projected area ratio, which is defined as the midplane. The point equidistant from the midplane to P_T is designated as P_C, which serves to distinguish cavity features from non-cavity regions. The integral of the curve from P_B to P_C can be utilized to characterize the cavity region. Fig. 15(b) shows the contour map corresponding to the three-dimensional surface topography. Contour maps are

used to characterize the three-dimensional topography of the cutting surface.

By calculating the projected area between adjacent contours, changes in surface features can be analyzed. Assuming the cutting surface is divided into n discrete height levels in the height direction, the projected area h_i of each level S_i is calculated as follows:

$$S_{\text{total}} = \sum_{i=1}^{n} S_i \tag{10}$$

where S_{total} is the total projected area. The projected area ratio is defined as:

$$\eta_i = \frac{S_i}{S_{\text{total}}}, i = 1,2,\ldots,n \tag{11}$$

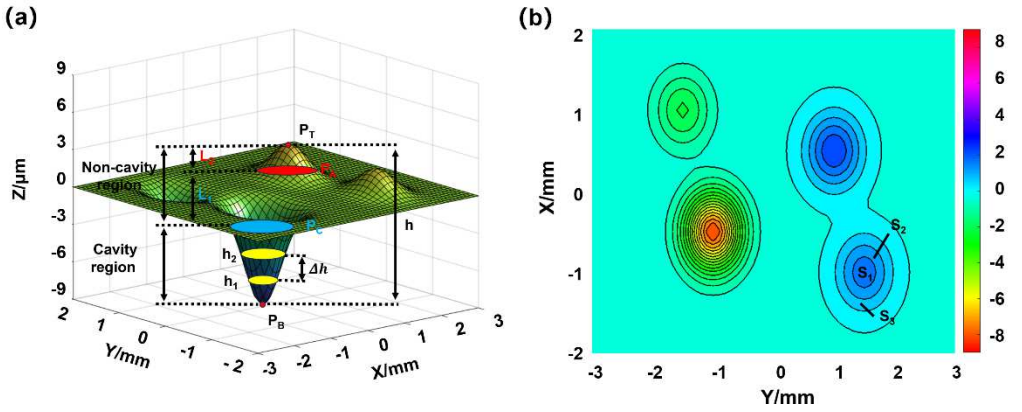


Fig. 15 Schematic diagram of cavity defect characterization((a) surface topography (b) contour map)

The cutting surface may contain multiple enclosed regions, which require accurate segmentation and area calculation. Once identified as a concave polygon, it is segmented into multiple convex polygons. The projected area of each segmented convex polygon is calculated using the following formula:

$$S_{\text{convex}} = \frac{1}{2}\sum_{i=1}^{m}\left(x_i y_{i+1} - x_{i+1} y_i\right) \tag{12}$$

where m is the number of vertices.

The total contour height S_t of the cutting surface refers to the vertical distance between the highest point P_T and the lowest point P_B:

$$S_t = P_T - P_B \tag{13}$$

Fig. 16(a) depicts the proportion of the projected area on the base plane at different contour heights; and Fig. 16(b) illustrates the cumulative distribution of the projected area on the base plane across various contour heights. By processing the curve generated from the cutting surface data points, evaluation metrics for the cavity characteristics of the cutting surface can be further extracted, providing a basis for surface quality assessment.

The cutting surface may exhibit features such as cavities, which typically cause localized height variations. To account for the influence of cavity features, the cavity feature contour height s_{ic} is introduced, obtained by subtracting the height of non-cavity regions from the total contour height:

$$S_{ic} = S_t - L_1 - L_2 \tag{14}$$

where L_1 is the vertical distance from the midplane to the surface peak, and L_2 is the vertical distance from the midplane to the bottom of the non-cavity region. Based on the analysis of the relationship curve between the projected area ratio and contour height using the three-dimensional point cloud collected from the surface profile, it is found that L_1 is approximately equal to L_2. Therefore, L_1 can be considered equal to L_2. Thus, it can be simplified as:

$$S_{ic} = S_t - 2L \tag{15}$$

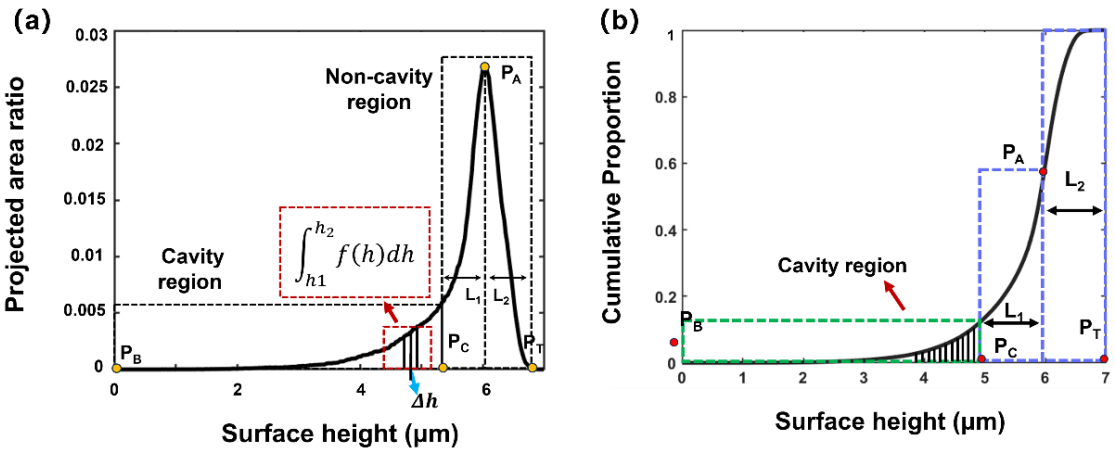


Fig. 16 Schematic diagram of cavity defect characterization
((a) projected area ratio (b) cumulative proportion)

Surface roughness is one of the key indicators for evaluating the quality of a machined surface, reflecting its microscopic characteristics. To calculate the surface roughness S_{as} of the machined surface, an integration method was employed. The calculation process is as follows:

$$S_{as} = \frac{1}{A_s}\sum_{i=0}^{m}\sum_{j=0}^{n}\left|h_{ij} - h'\right| \tag{16}$$

where h_{ij} is the height value of the machined surface point cloud data; h' is the reference plane of the machined surface; A_s is the projected area of the machined surface, equivalent to S_{total} as the area reference. This formula describes the height deviation of each point on the surface relative to the reference plane, and the surface roughness is calculated by summing these deviations.

For the additional roughness S_{asc} due to cavity features, the calculation formula is:

$$S_{asc} = \frac{1}{A_s}\sum_{i=1}^{m} S_i\left(h_i - h'\right) \tag{17}$$

where h_i is the contour height of the i-th layer, and h_{ic} is the height of cavity bottom.

3.1.2 Comparison of evaluation indicators

Following the completion of cutting under conventional and laser-assisted conditions, the machined surface data were respectively processed and analyzed. As depicted in Fig. 17, a comparison of surface evaluation indices under the two conditions is presented, with the first index being the relationship curve between the projected area ratio of contour intervals and

contour height. A comparison of the two figures reveals that the proportion of the cavity region under laser-assisted conditions is significantly reduced, accompanied by gentler height variations, indicating a substantial decrease in defects such as particle detachment and a smoother surface. This demonstrates the feasibility and superiority of processing aluminum matrix silicon carbide under laser-assisted thermal conditions.

The second index is the cumulative distribution plot of surface height, reflecting the frequency distribution of different heights and the proportion of cavity regions, thereby facilitating the analysis of surface quality and the characterization of surface cavity defects. Under conventional conditions, the proportion of cavity regions is relatively large, with the x-axis ranging from 0 to 7 μm, whereas under laser-assisted conditions, the *x*-axis range is 0 to 5 μm, indicating a more uniform surface height distribution and a significant reduction in cavity defects. Analysis of the slope variations in the curves shows that the maximum slope under conventional conditions occurs at 6 μm, while under laser-assisted conditions, it occurs at 4.3 μm with a notably larger value compared to conventional conditions, demonstrating a smoother surface height distribution under laser-assisted conditions.

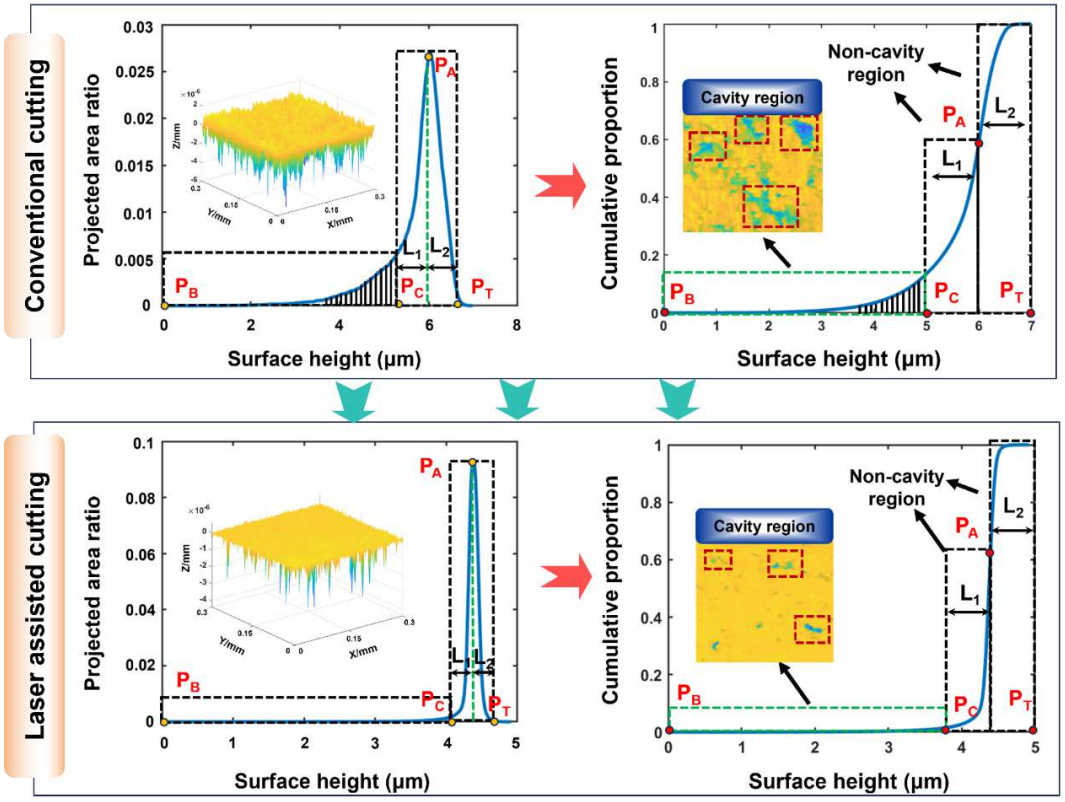


Fig. 17 Schematic diagram of surface quality evaluation metrics

3.2 Surface evaluation indicators analysis

Surface height parameters (*Sa* and *Sz*), cavity depth, and cavity surface roughness were employed to quantitatively evaluate the surface integrity. Figure 18 summarizes the effects of spindle speed, cutting depth, and feed rate on the surface morphology under conventional cutting and laser-assisted machining conditions. Across all investigated parameter ranges, laser-assisted machining consistently yields superior surface quality compared with conventional cutting. Under conventional cutting conditions, *Sa* varies between 0.32–0.56 μm and *Sz* between 7.1–10.1 μm depending on the cutting parameters. In contrast, under laser-assisted

machining conditions, *Sa* is significantly reduced to 0.023–0.051 μm, while *Sz* decreases to 4.0–6.1 μm. The substantial improvement is predominantly ascribed to laser-induced heat-mediated softening of the aluminum matrix, which alleviates stress concentration along the particle–matrix boundary, and suppresses particle pull-out and secondary abrasion mechanisms, as discussed in Section 2.

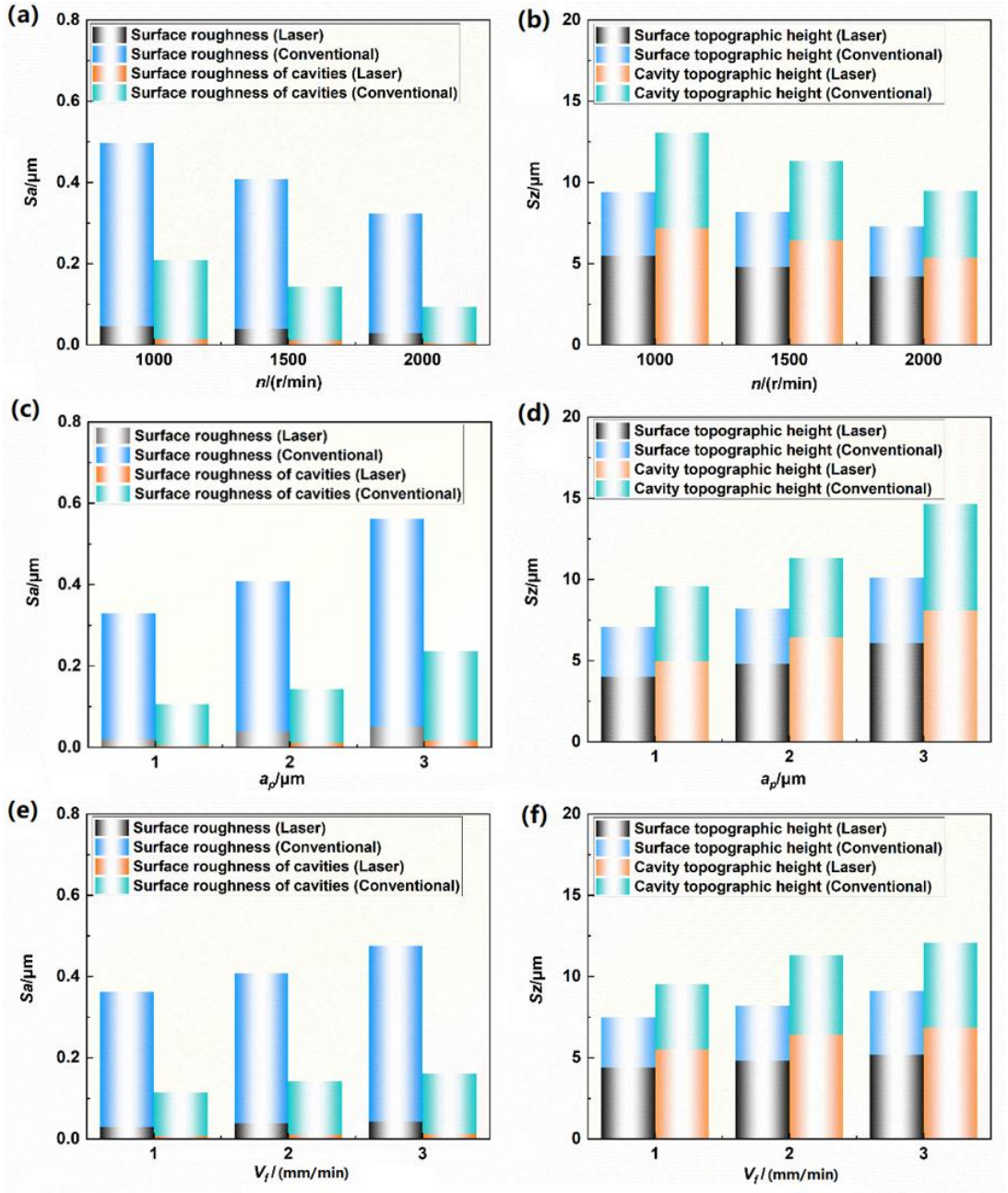


Fig. 18 Influence of cutting parameters on surface quality of SiCp/Al composites ((a)(b) a_p=2μm, v_f=2mm/min (c)(d) n=1500r/min, v_f=2mm/min (e)(f) n=1500r/min, a_p=2μm)

The influence of spindle speed on surface morphology is presented in Figs. 18(a–b) at a cutting depth of 2 μm and feed rate of 2 mm/min. Higher rotational speed shortens the tool-workpiece contact time and reduces effective friction, thereby suppressing built-up edge formation and limiting surface ploughing. Under laser-assisted machining conditions, the reduction in roughness is more pronounced, indicating that thermally enhanced matrix plasticity

further stabilizes the surface generation process at elevated speeds.

The variation in surface quality with cutting depth is shown in Figs. 18(c–d) at a spindle speed of 1500 r/min and feed rate of 2 mm/min. At smaller depths, material removal is dominated by ductile shearing of the aluminum matrix. With increasing depth, higher compressive and shear stresses develop at the tool–particle interface, promoting interfacial debonding, particle fracture, and matrix tearing. The resulting cavity formation and subsurface damage contribute directly to increased topographic height variation. Although laser-assisted machining mitigates these effects through stress redistribution and reduced flow stress of the matrix, surface roughness remains highly sensitive to cutting depth, indicating that this parameter plays a dominant role in determining surface integrity.

The effect of feed rate shown in Figs. 18(e-f) at a spindle speed of 1500 r/min and cutting depth of 2 μm reveals a moderate increase in *Sa* and *Sz* with increasing feed rate. A larger feed rate increases undeformed chip thickness and instantaneous cutting forces, leading to enhanced stress fluctuations at the particle–matrix interface. These fluctuations promote localized micro-debonding and minor cavity formation, thereby deteriorating surface finish. However, compared with cutting depth, the influence of feed rate is relatively less significant within the investigated range. Under laser-assisted machining conditions, improved matrix plastic accommodation effectively dampens stress variations and reduces particle displacement, resulting in a more stable surface morphology.

4 Conclusion

To investigate the material properties, the quasi-static experiments and high-temperature Hopkinson bar tests were conducted. A laser-assisted experimental platform is established to explore the three-dimensional topographic characteristics of optical surfaces. The primary conclusions are as follows:

(1) A micro-scale finite element model was developed to elucidate the material removal mechanism. Results reveal that conventional cutting induces severe stress concentrations, leading to massive interfacial debonding, catastrophic particle pull-out, and secondary ploughing. Conversely, laser-induced matrix softening homogenizes contact stresses and mitigates peak interfacial shear. This effect preserves interfacial anchoring, successfully transitioning the removal mode from macroscopic pull-out to controlled localized fracture, thereby fundamentally suppressing cavity defects and enhancing overall surface integrity.

(2) A high-precision surface point cloud map was reconstructed using an interpolation algorithm, and cavity defects on the machined surface were characterized using the projected area ratio method between contour intervals. The influence of process parameters on cavity defects, ranked from highest to lowest, is cutting depth, spindle speed, and feed rate, thereby providing a theoretical basis for prioritizing parameter adjustments in practical machining.

(3) The optimal processing window for achieving nanometric surface roughness was identified. The experimental results demonstrate that a spindle speed of 1500–2000 r/min, a cutting depth of 1–2 μm, and a feed rate of 1–2 mm/min under a 50 W laser power, yielded the best machining quality. Within this range, the laser-induced thermal softening effectively suppresses the brittle fracture of particles while avoiding surface ablation, reducing the surface roughness *Sa* to 0.023 μm.

Author contribution

Peng Gu: responsible for proposing the over-all research idea, creating the charts and graphs, and drafting and revising the manuscripts. Zhongjin Luo: reviewed the manuscript and provided revision suggestions. Daojie Hu: revised the charts and graphs, and provided revision suggestions for the manuscript. Andrea Mura: provided revision suggestions for the manuscript. Chengcheng Sun: provided revision suggestions for the manuscript. Chuanmin Zhu: translate relevant materials. Xiangjun Liu: reviewed the manuscript, and provided funding for the research through a grant.

All authors read and approved the final manuscript.

Funding

This work was supported by the National Natural Science Foundation of China (Grant No. 52305489), and the Open fund for the State Key Laboratory of Intelligent Manufacturing Equipment and Technology (Grant No. IMETKF2023017).

Availability of data and materials

The data that support the results of this article are included within the article.

Declarations

Competing interests The authors declare no competing interest.

Reference

[1] Huang S, Guo L, He H, et al. Experimental study on SiCp/Al composites with different volume fractions in high-speed milling with PCD tools[J]. International Journal of Advanced Manufacturing Technology, 2018, 97(5-8): 2731-2739.

[2] Huang S, Guo L, He H, et al. Study on characteristics of SiCp/Al composites during high-speed milling with different particle size of PCD tools[J]. International Journal of Advanced Manufacturing Technology, 2018, 95: 2269-2279.

[3] Zhang K, Gao Q, Yin X, et al. Study on grinding process and surface defects of SiCp/Al with 20% volume fraction[J]. Journal of Mechanical Science and Technology, 2024, 38(7): 3391–3401.

[4] Gu P, Zhu C, Tao Z, et al. A grinding force prediction model for SiCp/Al composite based on single-abrasive-grain grinding[J]. International Journal of Advanced Manufacturing Technology, 2020, 109(5-6): 1563-1581.

[5] Wang Y, Liao W, Yang K, et al. Investigation on cutting mechanism of SiCp/Al composites in precision turning[J]. International Journal of Advanced Manufacturing Technology, 2019, 100: 963-972.

[6] Xiang J, Xie L, Gao F, et al. Diamond tools wear in drilling of SiCp/Al matrix composites containing copper[J]. Ceramics International, 2018, 44(5): 5341-5351.

[7] Cui Y, Gao S, Wang F, et al. Study on the high-speed milling performance of high-volume fraction SiCp/Al composites[J]. Materials, 2021, 14(15): 4143.

[8] Chen S, Lu M, Lin J, et al. Finite element and experimental analysis of surface integrity and surface roughness of precision machining SiCp/Al composites[J]. Journal of Reinforced Plastics and Composites, 2024, 44(19-20): 1223-1237.

[9] Lu S, Li Z, Zhang J, et al. Finite element investigation of the influence of SiC particle distribution on diamond cutting of SiCp/Al composites[J]. Nanomanufacturing and Metrology, 2020, 3(4): 251-259.

[10] Kalantari O, Jafarian F, Fallah M. Comparative investigation of surface integrity in laser assisted and conventional machining of Ti-6Al-4V alloy[J]. Journal of Manufacturing Processes, 2021, 62: 90-98.

[11] Liu D, Li C, Xu P, et al. SiCp/Al composites from conventional to empowered machining: Mechanisms and processability[J]. Composite Structures, 2024, 346: 118433.
[12] Xu D, Liao Z, Axinte D, et al. Investigation of surface integrity in laser-assisted machining of nickel based super alloy[J]. Materials & Design, 2020, 194: 108851.
[13] Kim J, Kang B. Machining characteristics of micro lens mold in laser-assisted micro-turning[J]. Journal of Mechanical Science and Technology, 2018, 32(4): 1769-1774.
[14] Huang K, Shen Z, Zheng Z, et al. Investigation on the machinability of nitriding mold steel by applying in-situ laser assisted diamond cutting[J]. Journal of Manufacturing Processes, 2022, 84: 149-161.
[15] Liu Z, Lin B, Liang X, et al. Study on the effect of laser-assisted machining on tool wear based on molecular dynamics simulation[J]. Diamond & Related Materials, 2020, 109: 108022.
[16] Zhang C, Cao Y, Jiao F, et al. Research on cutting force characteristics of laser ultrasonically assisted turning of cemented carbide[J]. International Journal of Refractory Metals and Hard Materials, 2024, 122: 106726.
[17] Erdenechimeg K, Jeong H, Lee C. A study on the laser-assisted machining of carbon fiber reinforced silicon carbide[J]. Materials, 2019, 12(13): 2061.
[18] You K, Fang F, Yan G. Surface generation of tungsten carbide in laser-assisted diamond turning[J]. International Journal of Machine Tools and Manufacture, 2021, 168: 103770.
[19] Cui F, Zhang H, Yang M, et al. Laser-assisted machining of SiCp/Al composites: Preheating history driven microstructure evolution and its role in material removal[J]. Journal of Materials Processing Technology, 2025, 344: 119024.
[20] Lu X, Xv K, Wang X, et al. Modeling of laser-assisted micro-milling Inconel718 [J]. Precision Engineering, 2024, 88: 854-866.
[21] Mabrouki T, Girardin F, Asad M, et al. Numerical and experimental study of dry cutting for an aeronautic aluminium alloy. International Journal of Machine Tools and Manufacture, 2008, 48(11): 1187-1197.
[22] Wang T, Xie L. Simulation study on defect formation mechanism of the machined surface in milling of high volume fraction SiCp/Al composite[J]. The International Journal of Advanced Manufacturing Technology, 2015, 79(5-8): 1185-1194.
[23] Gu P, Zhu C, Tao Z, Yu Y. Micro-removal mechanism of high volume fraction SiCp/Al composite based on cohesive theory. International Journal of Advanced Manufacturing Technology, 2021, 117(1-2): 243-265.